FOSSEE, IIT Bombay
OpenFOAM Case Study Project
June 15, 2025

Dynamics of solids connected by liquid bridges with contact angle hysteresis

Rajnish Kaushal[1], Manjil Sitoula[2], and Amol Subhedar[3]

[1] Bachelor of Technology, National Institute of Technology, Kurukshetra
[2] Bachelors in Aerospace Engineering, Pulchowk Campus, Institute of Engineering, Tribhuvan University
[3] Assistant Professor, Department of Chemical Engineering, Indian Institute of Technology Bombay

Abstract

This report presents a comprehensive analysis of two-dimensional (2D) computational fluid dynamics (CFD) simulations conducted using the OpenFOAM interFOAM solver. The primary focus is on multiphase flow phenomena, with a particular emphasis on the intricate dynamics of contact angle hysteresis. The central investigation involved a rotating cylinder immersed in a two-fluid system, where two distinct contact angle hysteresis models were implemented: a static advancing/receding angle model and a dynamic feedback deceleration technique. To ensure the robustness and accuracy of the numerical methodology, three critical benchmark cases were performed. These included a squeezing flow problem, a Stokes drag comparison, and an analysis of Laplace pressure drop for a cylindrical droplet. The simulations achieved successful validation against established analytical solutions and theoretical principles. Specifically, the squeezing flow benchmark demonstrated the breakdown of lubrication theory at higher Reynolds numbers, while the Stokes drag comparison affirmed the Galilean invariance principle in low-Reynolds-number flows, and the Laplace drop test affirmed the Laplace pressure drop across an interface.

1 Introduction

Liquid bridges, small volumes of liquid held between two or more solid surfaces or particles by capillary forces, are a ubiquitous phenomenon encountered across a vast spectrum of natural and technological settings. Their presence is fundamental to processes in printing technologies, such as inkjet and offset printing, where controlled liquid transfer is paramount. They play crucial roles in adhesion, tribology, microfluidic devices, and even in large-scale industrial applications like oil recovery. The electronics industry relies on understanding liquid bridge behavior for multilayer

inkjet printing in the fabrication of circuits, fuel cells, and solar panels. Beyond engineered systems, liquid bridges are integral to biological phenomena, influencing the adhesion mechanisms of insects and playing roles in various physiological processes. The behavior of these liquid structures is predominantly governed by interfacial phenomena, where surface tension and the wettability of the solid surfaces dictate their shape, stability, and dynamic response. The inherent tendency of liquid interfaces to minimize their surface area, a direct consequence of surface tension, is the primary cohesive factor maintaining the bridge. The broad relevance of liquid bridges, spanning from nanoscale interactions to macroscopic industrial processes, necessitates the development of accurate and robust predictive models to understand and control their behavior.

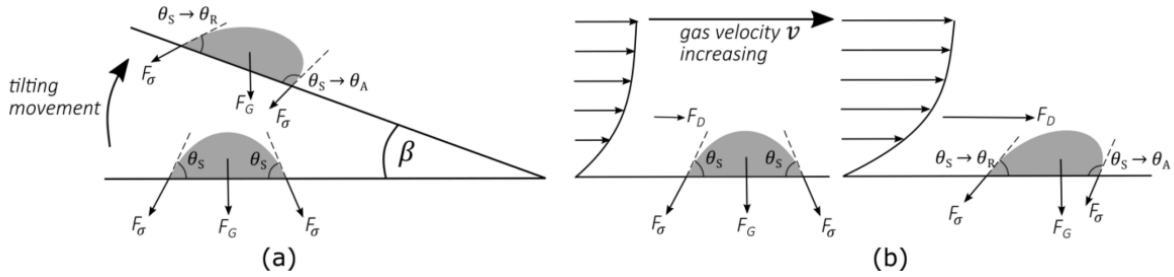

Figure 1: Schematic illustration of two different mechanisms causing the detachment of a sessile droplet and its subsequent movement along the solid surface Krämer et al. (2021)

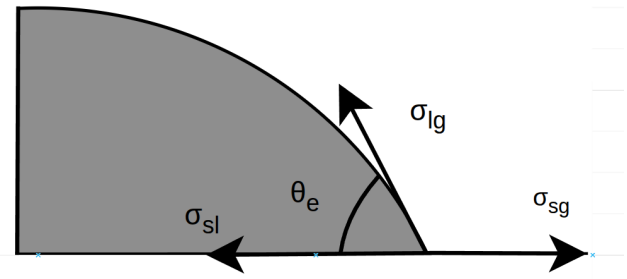

Figure 2: Schematics of the equilibrium contact angle according to Young

1.1 The Challenge of Contact Angle Hysteresis

While idealized models, such as that defining the equilibrium contact angle (θ_e) according to Young's equation for perfectly smooth and chemically homogeneous surfaces (Figure 2), assume a unique interfacial state, real-world solid surfaces invariably exhibit imperfections. These inherent imperfections, including surface roughness and chemical heterogeneity, give rise to the ubiquitous phenomenon known as contact angle hysteresis (CAH). CAH is characterized by a range of possible static contact angles for a given liquid-solid-vapor system, bounded by a maximum **advancing contact angle** (θ_A) and a minimum receding contact angle (θ_R). The advancing angle represents the highest possible angle observed just before the three-phase contact line moves over a previously dry area, whereas the receding angle is the lowest angle observed before the contact line retreats

from a previously wetted area. This hysteresis implies that the energy required to move a contact line is not constant, but rather depends on the direction of motion and the interface's history.

CAH is not merely a deviation from an ideal state; it is a critical physical factor that profoundly influences the behavior of liquid interfaces on real surfaces. It leads to the pinning of contact lines, a phenomenon where the interface can resist motion until applied forces are sufficient to overcome local energy barriers associated with surface defects. This pinning effect, illustrated by various mechanisms causing droplet detachment and movement (Figure 1), has significant consequences across numerous applications. These include, but are not limited to, the efficacy of self-cleaning coatings, the performance of waterproof materials, the resolution achievable in printing processes, and the controlled delivery of pharmaceutical agents. Therefore, the accurate inclusion of CAH in numerical simulations is often essential for achieving predictive accuracy, particularly in systems where contact line dynamics play a dominant role. The existence of multiple metastable energy states for an interface on a non-ideal surface, as indicated by CAH, means that the system's behavior can be history-dependent and more complex than predicted by models assuming a single equilibrium contact angle.

2 Problem Statement

The simulations encompass a primary case study and three complementary benchmark cases, all conducted within a 2D computational domain:" This is a very minor stylistic suggestion:

1. **Main Case: Rotating Cylinder with Contact Angle Hysteresis:** This simulation involves a 2D cylinder positioned centrally within a square domain, which is half-filled by one fluid and half by another. The core of this study lies in the application and analysis of two distinct contact angle hysteresis models, with a focus on the measured moments on the cylinder.

2. **Benchmark 1: Squeezing Flow Problem:** This case simulates an upper wall moving downwards, squeezing a fluid outwards. It was utilized to validate velocity and pressure profiles, as well as forces on the bottom wall, against lubrication theory. A key aspect was observing the theory's breakdown as Reynolds numbers increased.

3. **Benchmark 2: Stokes Drag Comparison:** This benchmark involved comparing the drag force on a 2D cylinder under two conditions: a stationary cylinder in a moving fluid, and a moving cylinder in a stationary fluid. This was performed to validate the reciprocity principle in low-Reynolds-number flows.

4. **Benchmark 3: Laplace Pressure Drop Analysis:** This case investigated the pressure difference across a 2D cylindrical droplet. The primary goal was to plot the pressure difference along a diameter and the average pressure difference over time, validating these against the Young-Laplace equation.

3 Governing Equations and Models

Multiphase flow involves the interaction of two or more immiscible fluids, presenting significant challenges in accurately simulating their dynamic interfaces. The Volume of Fluid (VOF) method,

a technique detailed in Rusche's work [5], is widely adopted for multiphase flow. It forms the core of the interFOAM solver used in these simulations for two-phase gas-liquid flow [3]. The VOF method tracks the interface by solving a transport equation for a phase fraction, denoted as α. In this formulation, α=1 represents one fluid (e.g., water), α=0 represents the other (e.g., air), and values between 0 and 1 indicate the presence of the interface.
The equations solved by interFoam are given as follows:
Continuity equation:

$$\nabla \cdot \mathbf{u} = 0 \tag{1}$$

Momentum equation:

$$\frac{\partial(\rho \mathbf{u})}{\partial t} + \nabla \cdot (\rho \mathbf{u}\mathbf{u}) = -\nabla p + \nabla \cdot (\mu(\nabla \mathbf{u} + (\nabla \mathbf{u})^T)) + \rho \mathbf{g} + \mathbf{f}_\sigma \tag{2}$$

where $\mathbf{u}$ is the velocity, p is the pressure, $\mathbf{g}$ is gravitational acceleration, and $\mathbf{f}_\sigma$ is the surface tension force.
Interface Capturing: Volume of Fluid (VOF), the interface is tracked by solving an advection equation for the volume fraction:

$$\frac{\partial \alpha}{\partial t} + \nabla \cdot (\alpha \mathbf{u}) + \nabla \cdot (\mathbf{u}_r \alpha(1-\alpha)) = 0 \tag{3}$$

Here, $\alpha = 1$ represents one fluid (e.g., liquid) and $\alpha = 0$ the other (e.g., gas). The interface is located in cells where $0 < \alpha < 1$. The final term is an artificial compression term to maintain a sharp interface, where $\mathbf{u}_r$ is a relative velocity field.
Surface Tension and Contact Angle, the surface tension force, $\mathbf{f}_\sigma$, is modeled using the Continuum Surface Force (CSF) model [2]:

$$\mathbf{f}_\sigma = \sigma \kappa \nabla \alpha \tag{4}$$

where σ is the surface tension coefficient and κ is the interface curvature, calculated as $-\nabla \cdot (\mathbf{n})$, with $\mathbf{n} = \frac{\nabla \alpha}{|\nabla \alpha|}$ being the interface normal vector.

4 Simulation Procedure

4.1 Geometry and Mesh

The geometry used in all cases is 2D, generated using the blockMesh utility of OpenFOAM, which is designed to create hexahedral meshes. Geometries for all cases are explained below as:

1. **Main Case: Rotating Cylinder with Contact Angle Hysteresis:** The domain is a square with dimensions 5 mm X 5 mm, fluid 1 fills the bottom half of the domain and fluid 2 fills the upper half. A cylinder wall is defined at the center of the domain. The domain is discretized with a total of 46,800 cells.

2. **Benchmark 1: Squeezing Flow Problem:** The domain is 100 mm long with an initial height of 5 mm, and the velocity of the upper wall moving downwards is 1 mm/s. The domain is discretized with 8,000 cells.

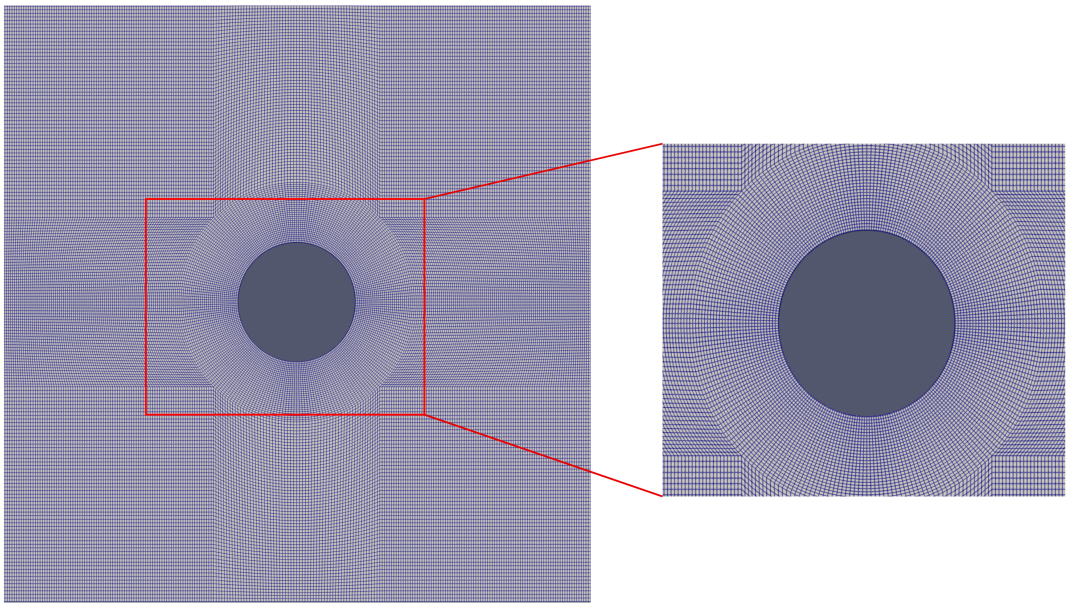

Figure 3: Discretized domain for the rotating cylinder problem

3. **Benchmark 2: Stokes Drag Comparison:** The domain is 400 mm X 50 mm, at the centre of which we have the cylinder over which forces are compared. The domain is discretized into 47,200 cells.

4. **Benchmark 3: Laplace Pressure Drop Analysis:** The domain for this case is 5 mm X 5 mm with a droplet of diameter 2 mm initialised at the centre of the domain. The domain is discretized with 90,000 cells.

4.2 Initial and Boundary Conditions

All of the initial and boundary conditions used are mentioned in Tables 1, 2, 3, and 4.

Boundary	**alpha.water**	**p_rgh**	**U**
leftWall	constantAlphaContactAngle	fixedFluxPressure	noSlip
rightWall	constantAlphaContactAngle	fixedFluxPressure	noSlip
topWall	zeroGradient	fixedFluxPressure	noSlip
lowerWall	zeroGradient	fixedFluxPressure	noSlip
cylinder	dynamicAlphaContactAngle	fixedFluxPressure	rotatingWallVelocity
front & back	empty	empty	empty

Table 1: Boundary Conditions for the Main Case

Boundary	alpha.water	pointDisplacement	p_rgh	U
leftWall	symmetryPlane	zeroGradient	symmetryPlane	symmetryPlane
rightWall	type: inletOutlet inletValue: uniform 0 value: uniform 0	zeroGradient	type: totalPressure p0: uniform 0	type: pressureInletOutletVelocity value: uniform (0 0 0)
lowerWall	zeroGradient	type: fixedValue value: uniform (0 0 0)	type: fixedFluxPressure value: uniform 0	noSlip
topWall	zeroGradient	type: timeVaryingUniformFixedValue value: uniform (0 0 0) file: "topWallDisplacement.dat"	type: fixedFluxPressure value: uniform 0	type: movingWallVelocity value: uniform (0 -0.001 0)
dFaces	empty	empty	empty	empty

Table 2: Boundary Conditions for Benchmark 1

Boundary	alpha.water	pointDisplacement	p_rgh	U
leftWall	zeroGradient	type: fixedValue value: uniform (0 0 0)	zeroGradient	type: fixedValue value: uniform (1e-7 0 0)
rightWall	type: inletOutlet inletValue: uniform 0 value: uniform 0	type: fixedValue value: uniform (0 0 0)	type: fixedValue value: uniform 0	type: inletOutlet uniform (1e-7 0 0)
lowerWall	zeroGradient	type: fixedValue value: uniform (0 0 0)	type: fixedFluxPressure value: uniform 0	noSlip
topWall	zeroGradient	type: fixedValue value: uniform (0 0 0)	type: fixedFluxPressure value: uniform 0	noSlip
cylinder	zeroGradient	type: timeVaryingUniformFixedValue value: uniform (0 0 0) file: "topWallDisplacement.dat"	type: fixedFluxPressure value: uniform 0	type: movingWallVelocity value: uniform (0 -0.001 0)
dFaces	empty	empty	empty	empty

Table 3: Boundary Conditions for Benchmark 2

Boundary	alpha.water	p_rgh	U
left	zeroGradient	fixedFluxPressure	noSlip
right	zeroGradient	fixedFluxPressure	noSlip
top	zeroGradient	fixedFluxPressure	noSlip
bottom	zeroGradient	fixedFluxPressure	noSlip
back	empty	empty	empty
front	empty	empty	empty

Table 4: Boundary Conditions for Benchmark 3

4.3 Solver and Numerical Schemes

Discretization	**Scheme**
Temporal	Euler
Gradient	Gauss linear
Laplacian	Gauss Linear corrected
Interpolation	Linear
snGrad	corrected
Specific Divergence Schemes:	
div(rhoPhi, U)	Gauss linearUpwind grad(U)
div(phi,alpha)	Gauss vanLeer
div(phirb, alpha)	Gauss interfaceCompression 1
div(((rho*nuEff)*dev2(T(grad(U)))))	Gauss linear

Table 5: Numerical Schemes used in the simulation

Parameter Description	**Symbol / Value(s)**	**Units**
Cylinder Radius	$R_{cyl} = 0.5$	mm
Density of fluid 1	$\rho_1 = 1000$	kg/m^3
Density of fluid 2	$\rho_2 = 1001$	kg/m^3
Viscosity of fluid 1	$\mu_1 = 1e-3$	$Pa.s$
Viscosity of fluid 2	$\mu_2 = 1e-3$	$Pa.s$
Surface Tension	$\sigma = 0.0001$	N/m
Advancing Angle	$\theta_A = 120$	$degrees$
Receding Angle	$\theta_R = 60$	$degrees$
Reynolds Number	$Re = 0.1$	$-$
Capillary Number	$Ca = 0.001$	$-$

Table 6: Parameters used in the simulation

The simulations were performed using the interFoam solver available in OpenFOAM, which is designed for two incompressible, isothermal, immiscible fluids. The choice of discretization schemes for the various terms in the governing equations is listed in Table 5. Table 6 lists the simulation parameters for the main case of rotating cylinder with CAH.

5 Results and Discussions

5.1 Benchmark Cases

5.1.1 Benchmark 1:

For the squeezing flow problem, the velocity and pressure distribution are calculated based on established lubrication theory principles [7]:

$$u(x,y) = \frac{6Vx}{h}\left(\frac{y}{h} - \frac{y^2}{h^2}\right) \tag{5}$$

$$p(x) = \frac{6\mu V}{h^3}\left(L^2 - x^2\right), \tag{6}$$

The normal and the viscous forces can be calculated using the equations given below:

$$F_{\text{normal}} = \frac{4\mu V L^3}{h^3} \tag{7}$$

$$F_{\text{viscous}} = \frac{3\mu V L^2}{h^2} \tag{8}$$

where V is the velocity of the top wall, x is the distance from the symmetry plane, y is the vertical distance from the bottom wall, h is the separation between the plates, L is the length of the plates, and μ is the dynamic viscosity of the fluid between the plates.

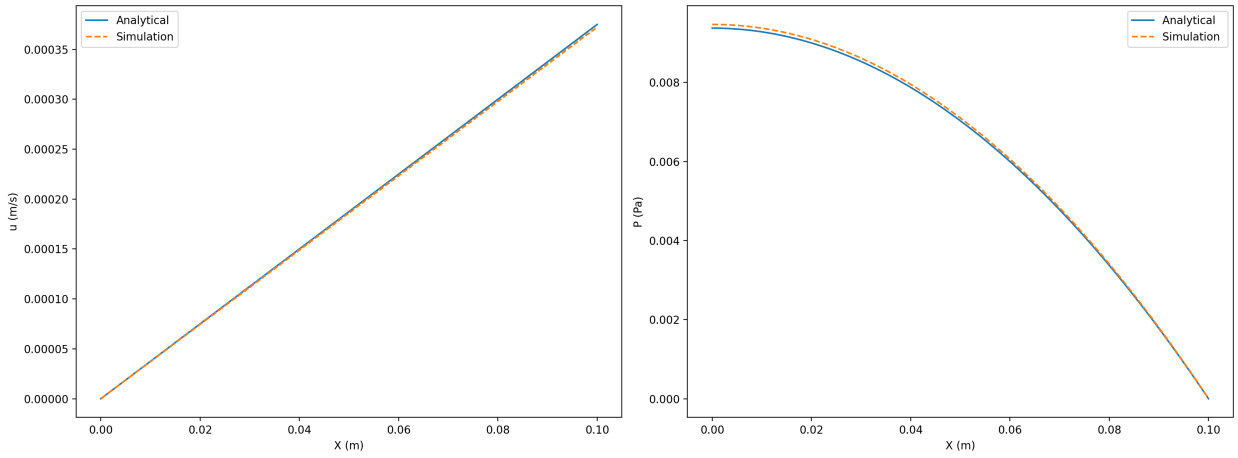

Figure 4: Maximum velocity (left) and pressure (right) along the length of the plates at t=1 sec for reference case

Systematic comparisons were performed between simulated velocity and pressure profiles and analytical solutions derived from lubrication theory. As expected, the velocity profiles across the gap exhibited a parabolic shape, characteristic of viscous flow between parallel plates. The pressure profiles along the plates showed a quadratic variation with a peak at the center. Figure 4 depicts the maximum velocity and pressure along the length of the plates at t = 1 sec. The total force exerted

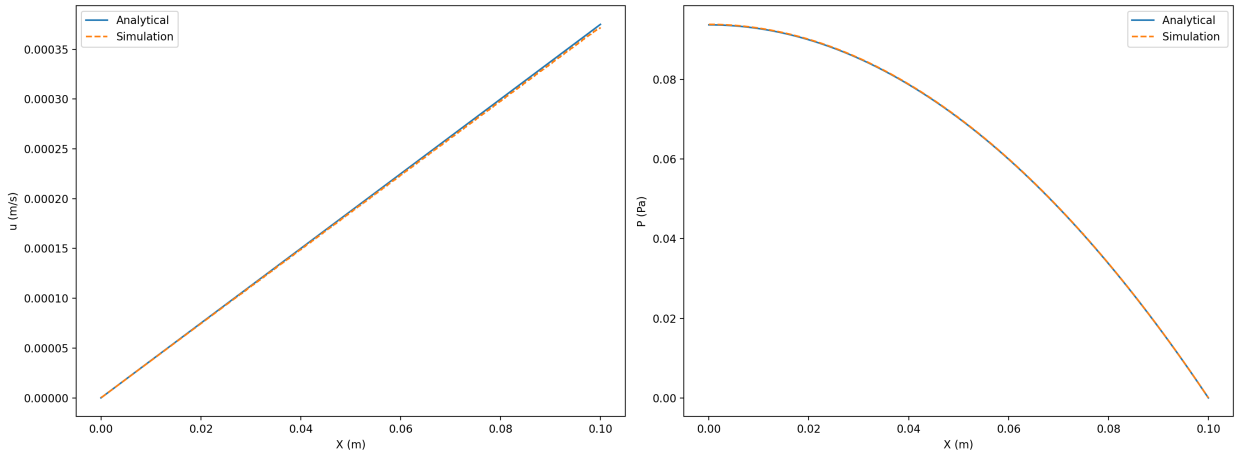

Figure 5: Maximum velocity (left) and pressure (right) along the length of the plates at t=1 sec for 10 times viscosity case

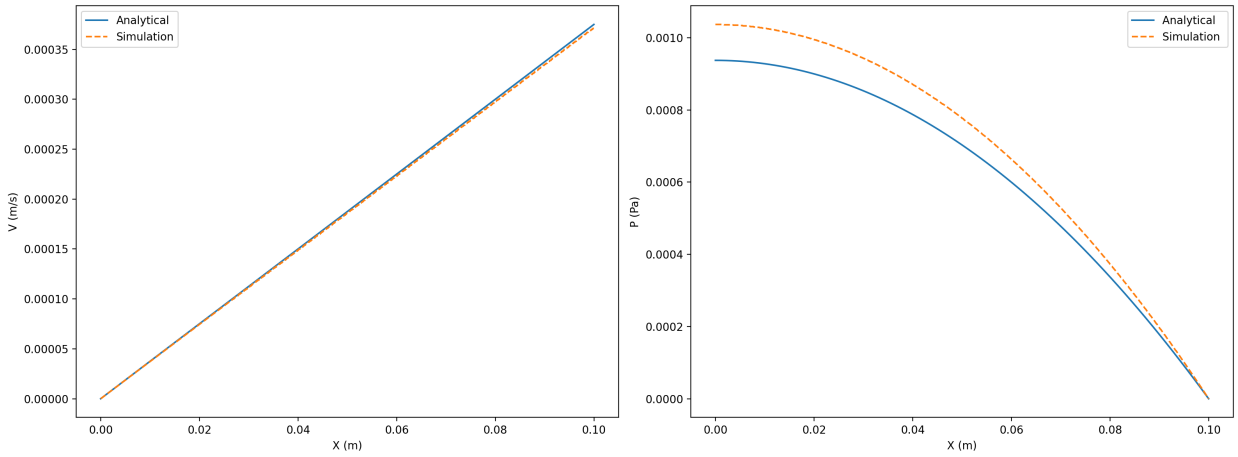

Figure 6: Maximum velocity (left) and pressure (right) along the length of the plates at t=1 sec for 1/10 times viscosity case

on the bottom wall was also quantitatively compared against analytical calculations (Table 8). For cases operating within the assumptions of lubrication theory, strong agreement was observed between the simulated and analytical results for these key parameters.

A crucial aspect of this benchmark was systematically investigating the limits of lubrication theory. We conducted simulations by varying the dynamic viscosity (μ) across a range of magnitudes, both increasing and decreasing. This directly impacted the Reynolds number (Re). Our analysis revealed a clear trend: cases with higher viscosity (and consequently lower Re) showed more accurate agreement with the analytical results from lubrication theory. Conversely, cases with lower viscosity (and thus higher Re) exhibited a significant divergence from the analytical values. Figures 5, 6, and 7 depict the maximum velocity and pressure along the length of the plates at t=1 sec for cases where viscosity is multiplied by factors of 10, 1/10, and 1/100, respectively.

This divergence directly stems from violating a fundamental assumption of lubrication theory:

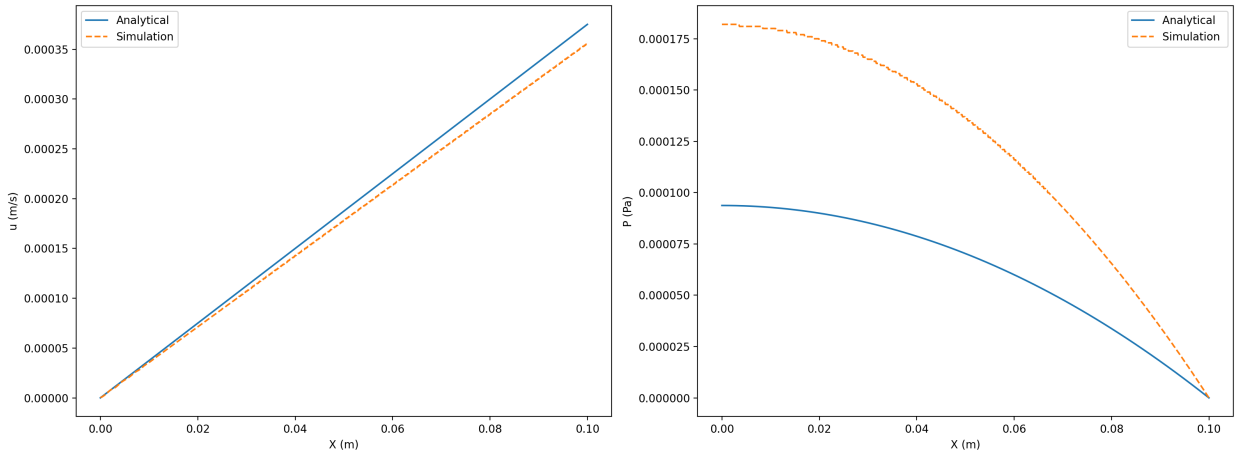

Figure 7: Maximum velocity (left) and pressure (right) along the length of the plates at t=1 sec for 1/100 times viscosity case

the dominance of viscous forces over fluid inertia, often stated as "negligible inertial effects." As the Reynolds number increases due to reduced viscosity, inertial forces become increasingly significant within the fluid flow and can no longer be neglected in the full Navier-Stokes equations.

Table 7 quantitatively summarizes the comparison between simulated and analytical results for the squeezing flow benchmark, illustrating the impact of varying Reynolds numbers.
This observation isn't a simulation failure; instead, it's a successful and powerful diagnostic validation of the analytical theory's limits. It demonstrates that interFOAM accurately captures the transition from a low-Re, viscosity-dominated regime (where lubrication theory applies) to a higher-Re, inertia-dominated regime (where the theory breaks down). This systematic variation of viscosity, and thus Reynolds number, provides a clear, quantitative demarcation of the Reynolds number regime where lubrication theory remains applicable and where it begins to lose validity for this specific squeezing flow problem. The results effectively map the boundaries of the theory's applicability, providing concrete numerical evidence. This robust validation not only confirms the simulation's accuracy within the theory's domain but also demonstrates its ability to accurately model physics outside that domain, emphasizing the value of CFD for situations where simplified analytical solutions are insufficient.

5.1.2 Benchmark 2: Stokes drag

The Stokes drag comparison benchmark was designed to validate interFOAM's accuracy in modeling fluid dynamics in the low Reynolds number regime, specifically testing the reciprocity principle, a fundamental concept in fluid dynamics and a manifestation of Galilean invariance [1]. Two distinct 2D scenarios were simulated involving a cylinder and a fluid:

1. **Scenario 1: Stationary Cylinder in Moving Fluid:** In this setup, a 2D cylinder was held fixed at a specific location within the computational domain. A uniform fluid flow was then introduced, moving past the stationary cylinder at a specified velocity.

2. **Scenario 2: Moving Cylinder in Stationary Fluid:** In this complementary setup, the 2D

Case	Peak Pressure (Analytical) (Pa)	Peak Pressure (Simulated) (Pa)	Peak Pressure (% Difference)
Ref. Case	0.009375	0.009468	0.9%
Viscosity 10 times	0.09375	0.093871	0.12%
Viscosity 1/10 times	0.0009375	0.001037	10.61%
Viscosity 1/100 times	0.00009375	0.000182	94.13%

Table 7: Comparison of Analytical and Simulated Peak Pressure and Force on Bottom Wall

	F_{normal} (N/m)	$F_{viscous}$ (N/m)
Analytical	0.000625	0.0000188
Simulation	0.000632	0.0000188

Table 8: Force comparison on the bottom wall for the reference case

cylinder was set to move at the same specified velocity through a fluid that was otherwise stationary throughout the domain.

For both scenarios, the fluid properties (density and viscosity) and the cylinder dimensions (radius) were kept identical. Crucially, the flow conditions were maintained such that the Reynolds number remained very low, ensuring the validity of the Stokes flow assumptions.

Scenario	Relative Velocity (m/s)	Calculated Drag Force (N/m)	Percentage Difference (%)
Moving Fluid, Stationary Cylinder	0.00005, at inlet	1.799628e-11	
Moving Cylinder, Stationary Fluid	0.0000748, cylinder velocity	1.843037e-11	2.41

Table 9: Comparison of Drag Force for Moving Fluid and Moving Cylinder Scenarios

The drag force exerted on the cylinder (per unit length, given the 2D nature of the simulations) was calculated for both Scenario 1 and Scenario 2. The computed drag forces in both cases were found to be nearly identical, with only minor discrepancies attributable to numerical precision. For Scenario 1 (moving fluid past a stationary cylinder), the fluid was initialized with a velocity of 0.00005 m/s. For Scenario 2 (moving cylinder in stationary fluid), the cylinder's velocity was

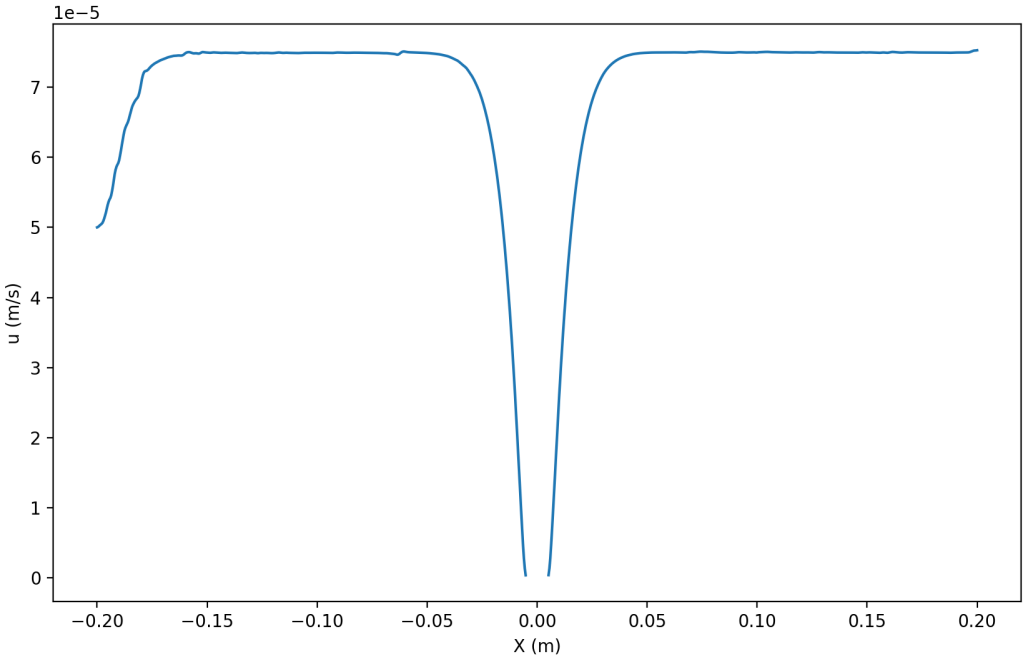

Figure 8: Velocity along the length of the domain for the moving fluid case

determined from the fully developed velocity profiles of Scenario 1, yielding a value of 0.0000748 m/s. Figure 8 depicts the velocity profile for the fixed flow case (Scenario 1) along the X-axis in the center of the domain.

This close agreement in drag forces between the two scenarios strongly validates Galilean invariance in Stokes flow. This fundamental principle asserts that, in the low Reynolds number regime where inertial effects are negligible, the drag force on an object depends solely on the relative velocity between the object and the fluid, rendering it fundamentally independent of the chosen reference frame. Consequently, identical drag forces are expected whether the cylinder moves through a stationary fluid or the fluid flows past a stationary cylinder, provided the same relative velocity is maintained.

The simulation results robustly confirm this fundamental principle. Table 9 presents a quantitative comparison of the calculated drag forces for the two Stokes drag scenarios, directly illustrating the Galilean invariance principle. The negligible difference in computed forces demonstrates interFOAM's ability to accurately model low-Reynolds-number flows where viscous forces dominate and inertial terms are effectively zero. This validation is critical because many capillary-driven flows, including aspects of the main rotating cylinder case, operate in regimes where velocities are small and viscous forces are paramount. Confirming the solver's accuracy in this fundamental regime builds confidence in the reliability of force and moment calculations in the main case, especially if the rotation speed is relatively low and surface tension effects are dominant. Any minor discrepancies observed could be attributed to extremely subtle residual inertial effects (if the Reynolds number was not absolutely zero), inherent numerical diffusion associated with the Volume of Fluid (VOF) method, or localized mesh resolution limitations near the cylinder surface.

5.1.3 Benchmark 3: Laplace Pressure Drop Analysis

This benchmark is crucial for verifying the accuracy of the surface tension implementation, specifically the Continuum Surface Force (CSF) model, and the associated calculation of interface curvature from the VOF field.
Laplace pressure refers to the pressure difference that exists across a curved interface separating two immiscible fluids. This pressure differential is a direct consequence of surface tension acting along the interface and its local curvature. The Young-Laplace equation, a cornerstone of capillarity [**?**], is the fundamental relationship that quantifies this pressure difference.. For a spherical interface, it is expressed as $\Delta p = 2\gamma/R$, where Δp is the pressure difference, γ is the interfacial tension, and R is the radius of curvature. For a 2D cylindrical droplet, assuming curvature only in the 2D plane, the equation simplifies to $\Delta p = \gamma/R$.
Table 10 provides a direct quantitative comparison between the simulated and theoretically predicted Laplace pressure for the cylindrical droplet.Figure 9 precisely illustrates the Laplace pressure drop across a fluid interface. It depicts the pressure variation along a droplet's diameter, clearly showing distinct, relatively constant pressure regions within each phase, separated by a sharp, discontinuous pressure jump at the liquid-vapor interface. This visual representation fundamentally confirms that surface tension creates a pressure difference across curved interfaces, a crucial physical reality for accurate multiphase flow simulations.

Parameter	**Value (Units)**
Interfacial Tension (γ)	0.07275 (N/m)
Droplet Radius (R)	0.001 (m)
Theoretical Laplace Pressure Difference ($\Delta p_{\text{theory}} = \gamma/R$)	72.75 (Pa)
Simulated Average Laplace Pressure Difference ($\Delta p_{\text{simulated}}$)	68.6 (Pa)
Percentage Difference	5.7 %

Table 10: Summary of Parameters and Calculated Values for Laplace Pressure Analysis

Any observed discrepancies were carefully analyzed. It is important to recall interFOAM's documented limitation regarding "imprecise predictions of the capillary-induced jump in pressure and the three-phase contact line" [6]. While this limitation suggests that perfect agreement may not be achievable at the highest precision, a good agreement (within acceptable engineering tolerances) would still demonstrate interFOAM's practical utility for problems dominated by surface tension. Conversely, significant errors would directly highlight this inherent numerical limitation, emphasizing areas where the solver's fidelity might be challenged. This benchmark is crucial for assessing interFOAM's ability to accurately resolve surface tension effects and the resulting pressure jumps across curved interfaces. It serves as a direct diagnostic for the fidelity of surface tension modeling within the solver, which is vital for the main rotating cylinder case where complex interface shapes and dynamic contact line behavior are expected, and where capillary forces will significantly influence the overall fluid dynamics and forces/moments on the cylinder.

5.1.4 Main Case: Rotating Cylinder with Contact Angle Hysteresis

The primary case study involved a 2D rotating cylinder positioned within a square computational domain. The domain was initially configured with two immiscible fluids: the lower half was filled

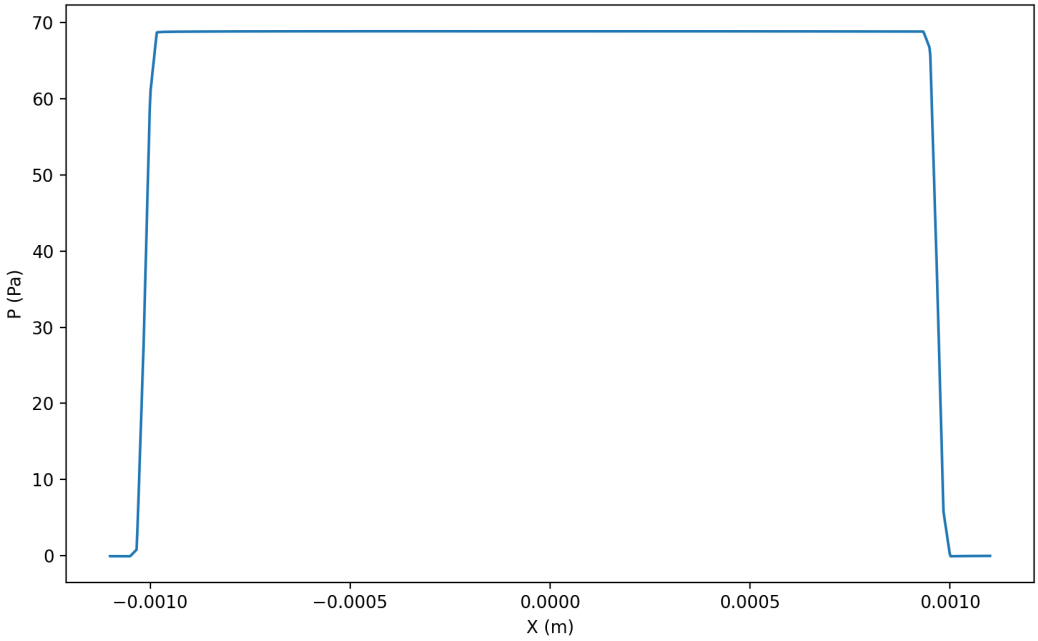

Figure 9: Pressure variation along the diameter of a droplet, illustrating the Laplace pressure drop.

with one fluid (e.g., water), and the upper half with another (e.g., air), creating a sharp horizontal interface at the mid-height. The 2D cylinder was precisely placed at the geometric center of this domain.
Two distinct contact angle hysteresis algorithms were implemented on the cylinder wall to capture the dynamic wetting behavior during rotation:

1. **Based on spatial coordinates:** This algorithm simplifies dynamic contact angle behavior by applying fixed advancing or receding angles based on face location relative to a **spatial threshold** (S_{thresh}). For a rotating cylinder, S_{thresh} spatially discriminates between advancing and receding interface regions on the surface. Here, the **cylinder's center** acts as this threshold, partitioning the cylinder into left (advancing for CCW rotation) and right (receding) regions. This direct spatial comparison offers a computationally efficient means to apply contact angle hysteresis, avoiding the complex calculation of local contact line velocity inherent to Volume of Fluid (VOF) simulations.
   Inputs for this algorithm are Advancing Contact Angle (θ_A), Receding Contact Angle (θ_R) and Spatial Threshold Coordinate (S_{thresh}).
   This algorithm follows the following procedure:

Algorithm 1: Spatially-Dependent Contact Angle Assignment with Hysteresis

Input: Threshold S_{thresh}, angles θ_A, θ_R
Output: Field of contact angles θ_F for each face

Initialization:
Initialize empty contact angle field θ_F;
Retrieve all face centers $\mathbf{c}_i$ from solid boundary patch;
foreach *face i on the solid boundary patch* **do**
    Extract spatial coordinate $S_{local} \leftarrow S(\mathbf{c}_i)$;
    if $S_{local} > S_{thresh}$ **then**
        $\theta_F[i] \leftarrow \theta_A$;
        `// Advancing angle`
    else
        $\theta_F[i] \leftarrow \theta_R$;
        `// Receding angle`
    end
end
return θ_F

2. **Feedback Deceleration Technique:** This more advanced dynamic model was implemented to allow the contact angle to adjust dynamically based on the contact line velocity, thereby ensuring pinning within the hysteretic range. The technique operates by increasing or reducing the contact angle by an increment directly proportional to the contact line velocity. A crucial aspect of this model's implementation was the determination of a "control coefficient," which needs to be chosen heuristically for the specific rotating cylinder case. The appropriate selection of this coefficient is vital for the model's stability and accuracy.

   This algorithm follows the following procedure:

Algorithm 2: Dynamic Contact Angle Assignment with Hysteresis and FDT Correction [4]

Input: θ_0 (static angle), θ_A, θ_R (advancing/receding angles in degrees), μ_{liquid} (viscosity), σ (surface tension), face phase fraction α_{patch}, velocity field $\mathbf{U}_p$

Output: Field of contact angles θ_F per face

Initialization:

Convert angles to radians: $\theta_{A,rad} \leftarrow \theta_A \cdot \pi/180$, $\theta_{R,rad} \leftarrow \theta_R \cdot \pi/180$;

Calculate the FDT constant:

$$C^* \leftarrow 10 \cdot \frac{(\theta_{A,rad} - \theta_{R,rad})}{|\cos(\theta_{A,rad}) - \cos(\theta_{R,rad})| + \text{VSMALL}} \cdot \frac{\mu_{liquid}}{\sigma}$$

Initialize empty contact angle field θ_F;

foreach *face i on the solid boundary patch* **do**

  Retrieve $\alpha_{face} \leftarrow \alpha_{patch}[i]$;

  if $10^{-6} < \alpha_{face} < 0.9999$ **then**

    `// Contact line is present`

    Compute current interface-wall angle θ_n from geometry;

    Compute $u_{wall} \leftarrow$ component of velocity $\mathbf{U}_p[i]$ parallel to wall;

    $\theta_{n+1} \leftarrow \theta_n$;

    if $\theta_n < \theta_{R,rad}$ **then**

      $\theta_{n+1} \leftarrow \theta_{R,rad}$;

    else if $\theta_n > \theta_{A,rad}$ **then**

      $\theta_{n+1} \leftarrow \theta_{A,rad}$;

    else

      $\Delta\theta \leftarrow C^* \cdot |u_{wall}|$;

      if $u_{wall} < 0$ **then**

        $\theta_{n+1} \leftarrow \theta_n - \Delta\theta$;

        `// Advancing`

      else if $u_{wall} > 0$ **then**

        $\theta_{n+1} \leftarrow \theta_n + \Delta\theta$;

        `// Receding`

      else

        $\theta_{n+1} \leftarrow \theta_n$;

      end

      Clamp: $\theta_{n+1} \leftarrow \min(\max(\theta_{n+1}, \theta_{R,rad}), \theta_{A,rad})$;

    end

    Convert back to degrees and set $\theta_F[i] \leftarrow \theta_{n+1} \cdot 180/\pi$;

  else

    $\theta_F[i] \leftarrow \theta_0$;

    `// Face is fully liquid or gas`

  end

end

return θ_F

Both algorithms yield highly comparable results, though they differ significantly in their practical utility. The spatial CAH model's application is limited to cases where the precise spatial demarcation of advancing and receding regions on the surface is predetermined. Conversely, the FDT approach provides a more versatile framework for CAH, extending its utility to general scenarios and crucially enabling the accurate representation of contact line pinning phenomena.

The initial interaction between the two immiscible fluids and the rotating cylinder is characterized by **contact line pinning**, a direct result of **contact angle hysteresis (CAH)** defined by $\theta_{adv} = 120^\circ$ and $\theta_{rec} = 60^\circ$. Pinning persists only until the viscous forces from the rotating cylinder exceed the local pinning forces. **Given the small Capillary number** ($Ca = 0.001$)**, significant pinning behavior would typically be expected.** However, in this simulation, contact line pinning is observed for an extremely short duration, often within unrecorded sub-time steps, primarily due to the high C^* value stemming from the chosen low surface tension ($\sigma = 0.0001$ N/m). As the cylinder rotates counter-clockwise ($\omega = 0.2$ rad/s), increasing interfacial shear stresses locally distort the interface, driving the contact angle towards its advancing value on one side and its receding value on the other. Upon reaching the critical depinning threshold, the contact line begins to propagate along the cylinder's surface. Table 11 showcases the evolving contact angles at the advancing and receding fronts at specific time steps during this CAH-dominated regime. The overall contact line movement reflects a complex balance among viscous drag, surface tension, and the governing contact angle hysteresis. Figure 10 depicts the domain at time t = 1.5 sec.The left panel depicts the phase fraction (red for fluid1, blue for fluid2), while the right panel illustrates the magnitude and direction of the velocity field

Time	Advancing Angle	Receding Angle
0.000155752	92.3981	82.2528
0.000192903	102.959	72.0421
0.000237483	110.621	64.7965

Table 11: Contact angles during the pinning of the contact line.

The transient behavior of the moment exerted on the rotating cylinder reveals a notable phenomenon (Figure 11). Initially, the moment acts in the counter-clockwise direction, aligning with and thus driving the cylinder's rotation. This initial 'promotive' moment is primarily attributed to the viscous shear stresses at the cylinder-fluid interface. As the cylinder commences rotation, it drags the adjacent fluid, generating a viscous torque consistent with the no-slip boundary condition and in the direction of rotation.

However, as simulation time progresses, the magnitude of this counter-clockwise moment steadily diminishes. Subsequently, a significant reversal in the moment's direction is observed, indicating that it now opposes the cylinder's rotation. Following this reversal, the moment eventually reaches a new steady state. This critical shift arises from the complex interplay among viscous forces, surface tension, and the dynamic evolution of the two-fluid interface under contact angle hysteresis. As the contact line moves and the interface deforms, the contribution of surface tension forces to the total moment becomes increasingly dominant. Unlike the initial viscous drag, the moment generated by the deformed interface, driven by the system's tendency to minimize interfacial energy, begins to counteract the rotational motion. The specific configuration of the

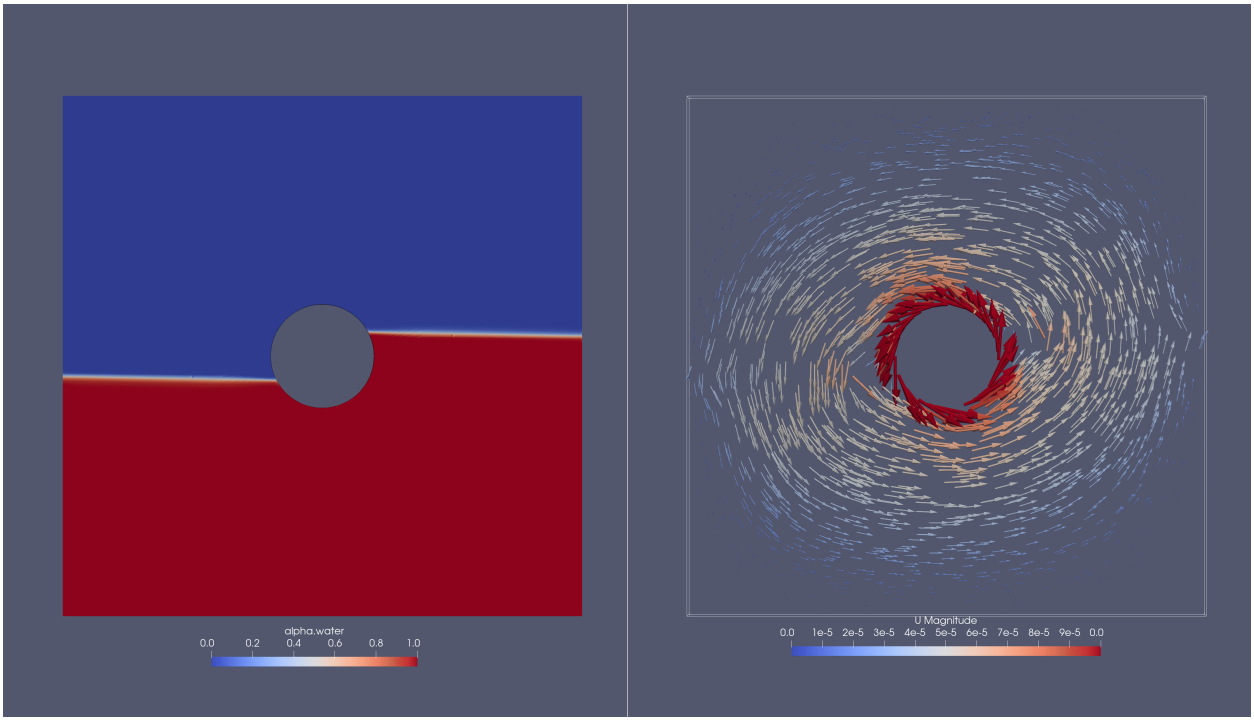

Figure 10: Rotating cylinder case at t=1.5 sec: Left: Phase fraction (red for fluid1, blue for fluid2); Right: Magnitude and direction of the velocity field.

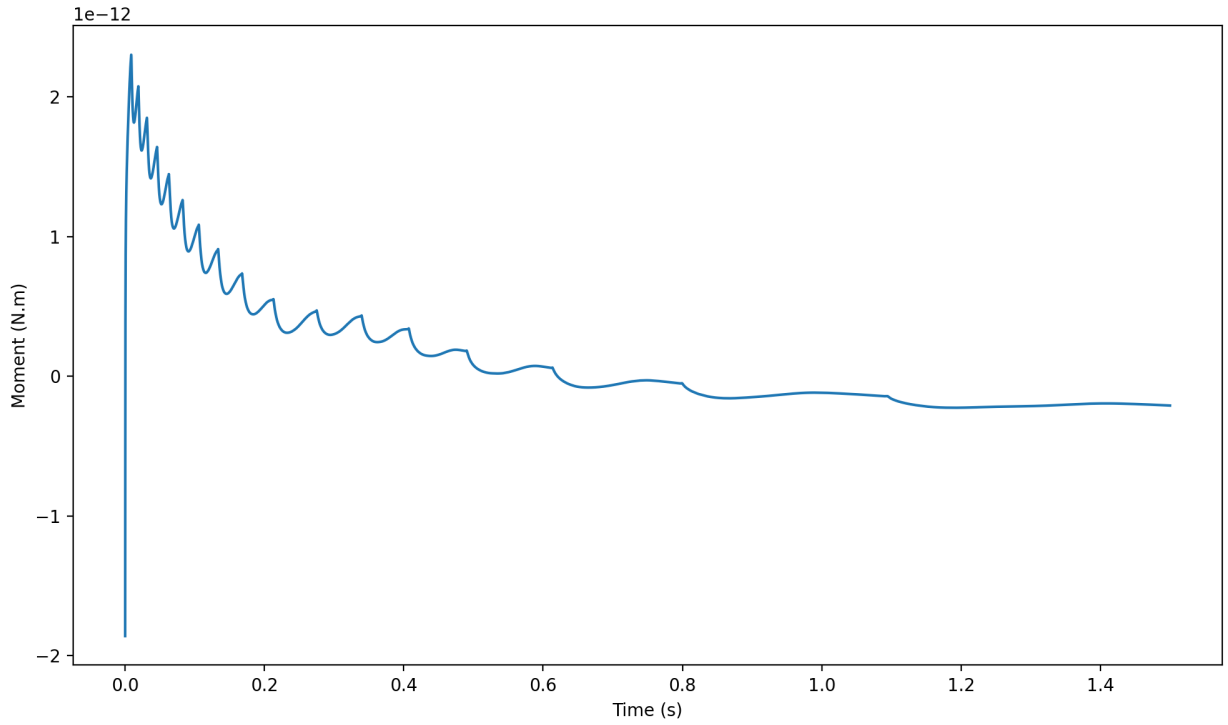

Figure 11: Moment on the cylinder plotted over time.

interface, influenced by the advancing and receding contact angles, leads to a net surface tension force that exerts a retarding torque on the cylinder. This transition underscores the dynamic competition between viscous forces (initially dominant and promoting rotation) and surface tension forces (which, after interface deformation, generate a significant opposing moment). The reversal in moment signifies the system's transition towards a new quasi-equilibrium state where the forces resisting rotation, largely due to the evolving interfacial configuration, become predominant.

6 Future Scope

Integration into Liquid Bridge Project: The validated hysteresis models and the insights gained from the rotating cylinder case should be integrated back into the broader "Dynamics of solids connected by liquid bridges" project. This could involve applying these models to simulations of actual liquid bridge formation, stability, and rupture, providing a more direct contribution to the project's core objectives.

7 Acknowledgment

I extend my sincere gratitude to Prof. Amol Subhedar for his insightful guidance and continuous encouragement during my FOSSEE internship. His weekly discussions and comprehensive guidance have been invaluable, and I am particularly grateful for his support in all situations, even those not directly related to the project. My deepest appreciation also goes to Manjil Sitoula for their exceptional mentorship, which was instrumental in the successful completion of this work. I am profoundly thankful to the FOSSEE team for their unwavering support and for offering this significant internship opportunity.

References

[1] George Keith Batchelor. *An introduction to fluid dynamics*. Cambridge university press, 2000.

[2] Jeremiah U Brackbill, Douglas B Kothe, and Charles Zemach. A continuum method for modeling surface tension. *Journal of computational physics*, 100(2):335–354, 1992.

[3] Suraj S Deshpande, Lakshman Anumolu, and Mario F Trujillo. Evaluating the performance of the two-phase flow solver interfoam. *Computational science & discovery*, 5(1):014016, 2012.

[4] Veronika Krämer, Beawer Barwari, Sebastian Burgmann, Martin Rohde, Simon Rentschler, Christopher Holzknecht, Christoph Gmelin, and Uwe Janoske. Numerical analysis of an adhering droplet applying an adapted feedback deceleration technique. *International Journal of Multiphase Flow*, 145:103808, 2021.

[5] Henrik Rusche. Computational fluid dynamics of dispersed two-phase flow at high phase fractions. *Ph. D. thesis, University of London*, 2002.

[6] Yuhang Wang, Wilko Rohlfs, and Reinhold Kneer. Effects of protuberant structure on coalescence-induced jumping of droplets on superhydrophobic surfaces. *Physics of Fluids*, 35(8), 2023.

[7] Frank M White and Joseph Majdalani. *Viscous fluid flow*, volume 3. McGraw-Hill New York, 2006.